**Detailed Methods**

The study workflow is shown in Figure 1. This study was retrospective but was conducted in a double-blind fashion, where the procedure operators were blinded to the simulation results, and those who performed image processing and simulation were blinded to the clinical results.

*Study Population.* We retrospectively evaluated the medical records of the patients who were referred to the Johns Hopkins Hospital between July 2006 and April 2011 for catheter ablation of VT. The study was approved by the Institutional Review Board of the Johns Hopkins Medical Institutions. Patients were included if the pre-ablation MRI with LGE showed myocardial scar. To avoid any possibility of confounding the data, patients were excluded if the pre-ablation MRI showed any artifacts within the heart, regardless of the size and the location, from an implantable cardioverter defibrillator (ICD) and/or the ICD leads.

*Pre-Ablation MRI.* Our MRI protocol for LGE has been described previously[1]. Briefly, the patients underwent cardiac MRI with LGE with a 1.5-T scanner (Avanto, Siemens Medical Solutions) with the standard 6-element cardiac phased-array receiver coil and the spine coil. Ten to 12 contiguous short-axis slices were prescribed to cover the entire left ventricle (LV). LGE images were acquired 15 to 30 minutes after an intravenous injection of a contrast agent (Magnevist, gadolinium diethylenetriaminepentacetate <Gd-DTPA>, Berlex) at 0.2 mmol/kg with a standard non-phase-sensitive inversion recovery sequence. Representative imaging parameters were as follows: repetition time 1 heartbeat (~ 700-1000 ms), echo time 3.32 ms, in-plane spatial resolution 1.5-1.9 mm, 8-mm slice thickness, 0-2-mm gap, inversion time 175 to 280 ms (adjusted to null the signal of normal myocardium), flip angle 25° and a gradient recalled echo (GRE) readout. Each image acquisition was ECG gated, and the image was acquired during

a single, typically end-expiration, breath hold. If the patient had an ICD, monitoring and tachyarrhythmia therapies (anti-tachycardia pacing/defibrillation) were turned off during the scanning[2, 3].

*Electrophysiology Study and Mapping.* Intracardiac electrograms were filtered at 50 to 500 Hz. Quadripolar electrode catheters (5 Fr) were introduced into the right femoral vein and advanced to the high right atrium, the His position, and the right ventricular (RV) apex. Programmed RV stimulation was performed in all patients with 1 to 3 extrastimuli to induce VT. Three-dimensional (3-D) electroanatomical mapping (CARTO, Biosense Webster, Diamond Bar, California) of the LV was performed with either a 4-mm tip ablation catheter (Navistar, Biosense Webster) or a 3.5-mm tip, open-irrigation ablation catheter (Thermocool, Biosense Webster). The ablation catheter was introduced to the LV by a transseptal approach via a femoral vein, and/or by a retrograde aortic approach via a femoral artery. A voltage map was generated during sinus rhythm, followed by activation. All VTs studied were hemodynamically unstable, precluding use of entrainment or activation mapping. An isthmus, or a central common pathway, of the VT circuit was identified by pace-mapping, where a match of the QRS morphology between the pace map and the VT was achieved. The location within the isthmus was estimated by the interval between the pacing stimulus and the onset of QRS complex on the surface ECG. Low voltage was defined as bipolar voltage amplitude $\leq$1.5 mV, and scar as bipolar voltage amplitude $\leq$0.5 mV[4]. Intraprocedural anticoagulation was achieved by multiple bolus injection of heparin to maintain an activated clotting time between 350 and 400 sec.

*Ablation.* RF energy was delivered at sites of origin as determined by the electrophysiology study and mapping. For non-irrigated catheters, the target temperature was set to 60°C; for irrigated tip catheters, the initial power setting was 30 W; applications of RF energy

were titrated to achieve an impedance decrease of 10 ohms. All VT morphologies were hemodynamically unstable, therefore the standard substrate modification was performed during sinus rhythm, where the exit sites, the central common pathways and multiple adjacent areas, particularly around the scar border, were ablated. After ablation, programmed stimulation was repeated. Acute success was defined as inability to induce clinical VT at the end of the procedure. If non-clinical VT morphologies were inducible, those were also ablated.

*Image Processing.* On each short-axis LGE image, the endocardial and epicardial contours of both the left and right ventricles were manually segmented, registered and volume-rendered in 3-D space to create a finite element mesh for computer simulation (Figure 1). An interpolation method based on spherical harmonic expansion was used to define the ventricular boundary[5, 6]. Signal intensity (SI) of the ventricular myocardium between the slices was reconstructed using layer-specific tricubic interpolation. The scar was defined as the myocardium with SI>50% of the maximal SI within the myocardium, and HZ was defined as the myocardium with SI>peak SI in the remote normal myocardium but <50% of maximal SI within the myocardium[1]. Myofiber orientation in the ventricles was estimated based on a modification of a rule-based method [7] where the transmural myofiber direction was assigned as a linear function of the distance from the endocardium to the epicardium, from +60° to -60°, respectively, with reference to the circumferential direction[8] (Figure 1). The transmural myolaminar sheet direction was fixed at -30° with reference to the radial direction[9].

*Electrophysiological Representation and Parameters.* Mathematical description of cardiac tissue was based on the monodomain representation[10], which involves the solution of a reaction-diffusion equation coupled to a system of ordinary differential equations describing membrane kinetics. The governing equations were:

$$C_m \frac{\delta V_m}{\delta t} + I_{ion} = \nabla \cdot (\sigma_i \nabla V_m)$$

$$I_{ion} = I_{ion}(V_m, \mu)$$

$$\frac{\delta \mu}{\delta t} = G(V_m, \mu)$$

where $\sigma_i$ is the intracellular conductivity tensor; $V_m$ is the transmembrane potential; $C_m$ is the membrane specific capacitance; and $I_{ion}$ is the density of the transmembrane current, which in turn depends on $V_m$ and on a set of state variables $\mu$ describing the dynamics of ionic fluxes across the membrane. In all infarcted ventricular models, scar was modeled as insulator (collagen). The intracellular conductivities, $\sigma_i$, were assigned values as in Bishop *et al.*[11], matching canine conduction velocities reported by Roberts *et al.*[12]. Within the HZ, the transverse conductivity was decreased by 90% to reflect Cx43 lateralization[13].

$I_{ion}$ of the non-infarct tissue was represented by the ten Tusscher model of the human ventricular tissue[14]. The same membrane model was also modified to represent the electrophysiology of HZ cells. Due to the lack of available human electrophysiological parameters, the parameters in the modification were derived from large animal models. Specifically, previous patch clamp studies using cells harvested from the epicardial border zone of infarcted canine hearts have reported a reduction in peak sodium current to 38% of the normal value[15]; in peak L-type calcium current to 31% of normal[16]; and in peak potassium currents $I_{Kr}$ and $I_{Ks}$ to 30% and 20% of the maximum[17], respectively. These modifications were implemented in the ten Tusscher model to obtain a HZ action potential; the latter was characterized with longer action potential duration, decreased upstroke velocity, and decreased peak action potential amplitude compared to that of the normal myocardium.

*Simulation Protocol and Analysis.* All simulations were performed using the software package CARP (CardioSolv, LLC) on a parallel computing platform, a 2,000-core Linux cluster; the numerical methodology has been described in previous publications[10, 18, 19]. We used sophisticated solver techniques, which ensure high efficiency, accuracy and stability of our numerical solutions for computational grids of the size of the human heart. Our spatial and temporal discretization steps are chosen specifically, after extensive testing, to achieve maximum performance while ensuring accuracy and convergence.

Programmed electrical stimulation (PES), similar to protocols used for clinical evaluation, was simulated in all patients with 1 to 3 extrastimuli to induce VT in simulation. PES was performed from the RV apex and the RV outflow tract. The models were paced from an endocardial location for 6 beats (S1) at a cycle length of 350ms followed by a premature stimulus (S2) initially given at 90% of S1 cycle length. The timing between S1 and S2 was progressively shortened until VT was induced. If VT was not induced, a second premature stimulus (S3) was delivered after S2. A 500 millisecond-episode of activity in the multiscale monodomain model with a grid of 5.4 million elements typically took 3 hours to run on 15 nodes.

VT circuits were analyzed on both the endocardial and epicardial surfaces. Lines of conduction block were considered to occur between adjacent sites where wavefronts on opposite sides of the line moved in different directions[20]. Lines of conduction block relevant to the VT circuits were drawn on the isochrone maps using a cubic spline interpolation function[21].

*Image Registration.* To compare successful ablation sites in the standard approach and the estimated optimal targets in the image-based simulation approach, the 3-D electroanatomical map of the LV was registered to the finite element mesh used in simulation. Rigid-body

transformation was conducted based on the heart geometry shell used in the standard approach that was derived from the pre-ablation MRI (CARTO-Merge). When CARTO-Merge was not used in the standard approach, rigid-body transformation was conducted based on anatomical landmarks including the LV apex, RV apex, aorta, mitral valve annulus, and RV outflow tract.

*Statistical analysis.* Continuous variables are presented as means ± SD, and categorical variables as numbers and percentages. Student's paired t-tests were performed to compare the extent of the estimated target region. A $P$ value<0.05 will be considered statistically significant. Statistical analysis was performed using Matlab (Statistical Toolbox, MathWorks, Inc, Natick, MA).

**References for Detailed Methods**


**1.** Schmidt A, Azevedo CF, Cheng A, et al. Infarct tissue heterogeneity by magnetic resonance imaging identifies enhanced cardiac arrhythmia susceptibility in patients with left ventricular dysfunction. Circulation 2007;115:2006-2014.

**2.** Nazarian S, Halperin HR. How to perform magnetic resonance imaging on patients with implantable cardiac arrhythmia devices. Heart Rhythm 2009;6:138-143.

**3.** Nazarian S, Hansford R, Roguin A, et al. A prospective evaluation of a protocol for magnetic resonance imaging of patients with implanted cardiac devices. Annals of internal medicine 2011;155:415-424.

**4.** Marchlinski FE, Callans DJ, Gottlieb CD, Zado E. Linear ablation lesions for control of unmappable ventricular tachycardia in patients with ischemic and nonischemic cardiomyopathy. Circulation 2000;101:1288-1296.

**5.** Hopenfeld B. Spherical harmonic-based finite element meshing scheme for modelling current flow within the heart. Med Biol Eng Comput 2004;42:847-851.

**6.** Ashikaga H, Sasano T, Dong J, et al. Magnetic resonance-based anatomical analysis of scar-related ventricular tachycardia: implications for catheter ablation. Circulation research 2007;101:939-947.

**7.** Bayer JD, Blake RC, Plank G, Trayanova NA. A Novel Rule-Based Algorithm for Assigning Myocardial Fiber Orientation to Computational Heart Models. Annals of biomedical engineering 2012.

**8.** Streeter DD, Jr., Spotnitz HM, Patel DP, Ross J, Jr., Sonnenblick EH. Fiber orientation in the canine left ventricle during diastole and systole. Circulation research 1969;24:339-347.

**9.** LeGrice IJ, Smaill BH, Chai LZ, Edgar SG, Gavin JB, Hunter PJ. Laminar structure of the heart: ventricular myocyte arrangement and connective tissue architecture in the dog. The American journal of physiology 1995;269:H571-582.

**10.** Plank G, Zhou L, Greenstein JL, et al. From mitochondrial ion channels to arrhythmias in the heart: computational techniques to bridge the spatio-temporal scales. Philosophical transactions 2008;366:3381-3409.

**11.** Bishop MJ, Plank G. Representing cardiac bidomain bath-loading effects by an augmented monodomain approach: application to complex ventricular models. IEEE transactions on bio-medical engineering 2011;58:1066-1075.

**12.** Roberts DE, Hersh LT, Scher AM. Influence of cardiac fiber orientation on wavefront voltage, conduction velocity, and tissue resistivity in the dog. Circulation research 1979;44:701-712.

**13.** Yao JA, Hussain W, Patel P, Peters NS, Boyden PA, Wit AL. Remodeling of gap junctional channel function in epicardial border zone of healing canine infarcts. Circulation research 2003;92:437-443.

**14.** ten Tusscher KH, Noble D, Noble PJ, Panfilov AV. A model for human ventricular tissue. American journal of physiology 2004;286:H1573-1589.

**15.** Pu J, Boyden PA. Alterations of Na+ currents in myocytes from epicardial border zone of the infarcted heart. A possible ionic mechanism for reduced excitability and postrepolarization refractoriness. Circulation research 1997;81:110-119.

**16.** Dun W, Baba S, Yagi T, Boyden PA. Dynamic remodeling of K+ and Ca2+ currents in cells that survived in the epicardial border zone of canine healed infarcted heart. American journal of physiology 2004;287:H1046-1054.

**17.** Jiang M, Cabo C, Yao J, Boyden PA, Tseng G. Delayed rectifier K currents have reduced amplitudes and altered kinetics in myocytes from infarcted canine ventricle. Cardiovascular research 2000;48:34-43.

**18.** Vigmond EJ, Hughes M, Plank G, Leon LJ. Computational tools for modeling electrical activity in cardiac tissue. Journal of electrocardiology 2003;36 Suppl:69-74.

**19.** Vigmond EJ, Weber dos Santos R, Prassl AJ, Deo M, Plank G. Solvers for the cardiac bidomain equations. Progress in biophysics and molecular biology 2008;96:3-18.

**20.** Dillon SM, Allessie MA, Ursell PC, Wit AL. Influences of anisotropic tissue structure on reentrant circuits in the epicardial border zone of subacute canine infarcts. Circulation research 1988;63:182-206.

**21.** Ciaccio EJ, Coromilas J, Costeas CA, Wit AL. Sinus rhythm electrogram shape measurements are predictive of the origins and characteristics of multiple reentrant ventricular tachycardia morphologies. Journal of cardiovascular electrophysiology 2004;15:1293-1301.

**Supplemental Figures**

**Supplemental Figure 1. Comparison between image-based simulation and standard approach (continued).** The figure structure is the same as in Figure 2. Two patients (patient a and b) underwent EPS without catheter ablation. The simulation result shows a unidirectional circus movement pattern. The simulation result is consistent with the 12-lead ECG of the clinical VT. One patient (patient c) underwent successful EPS and ablation, but VT was not inducible in simulation. This was a repeat ablation case who had undergone a previous ablation attempt for a focal, non-scar-related VT. The scale of the 12-lead ECG in the *Electrophysiology study* column is 100mm/s. (patient a, b and c).

**Supplemental Figure 2. Comparison between image-based simulation and standard approach (continued).** The figure structure is the same as in Figure 2. The simulation result shows a unidirectional circus movement pattern. The simulation result is consistent with the 12-lead ECG of the clinical VT. The scale of the 12-lead ECG in the *Electrophysiology study* column is 100mm/s.

Supplemental Figure 1

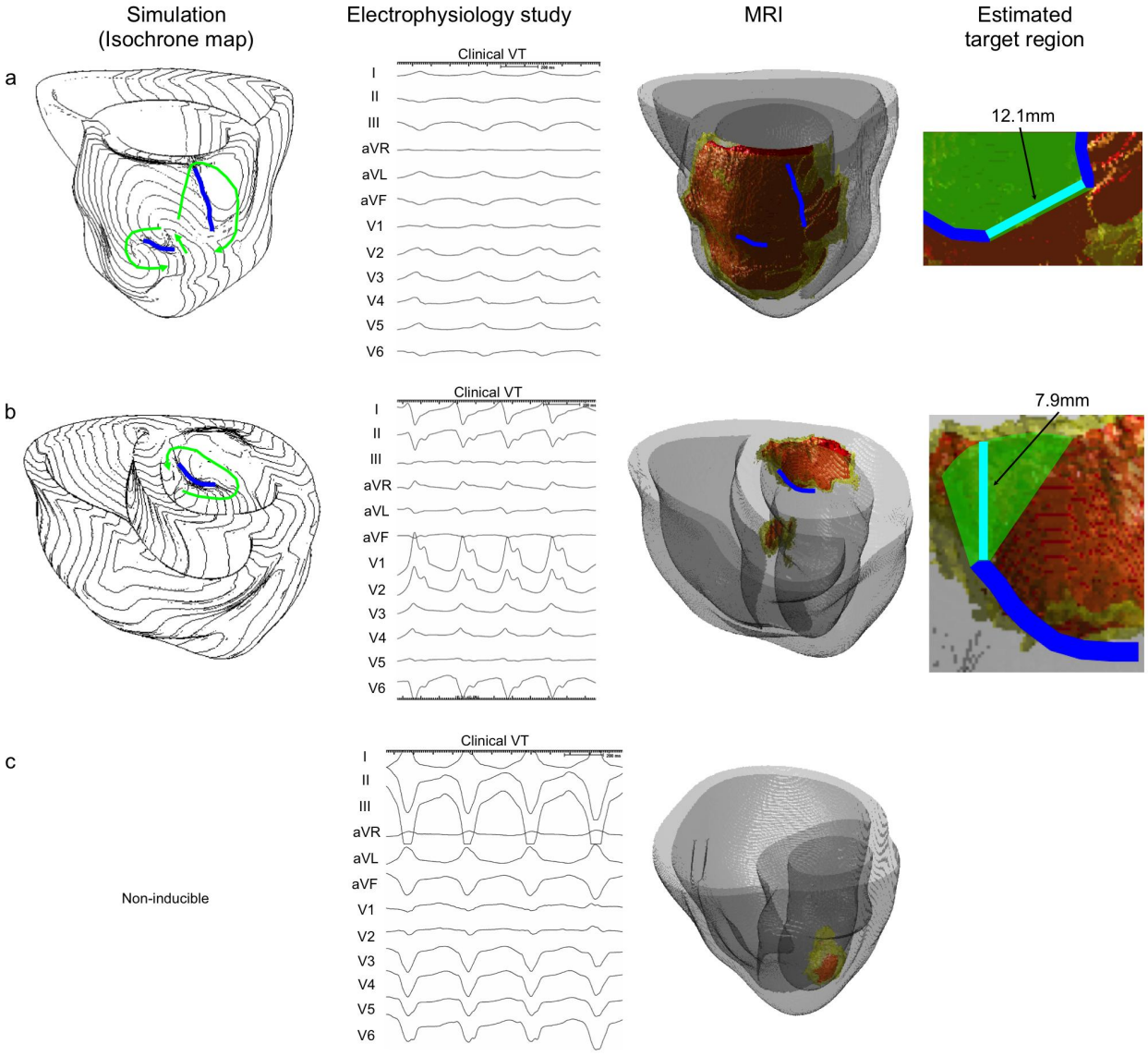

Supplemental Figure 2

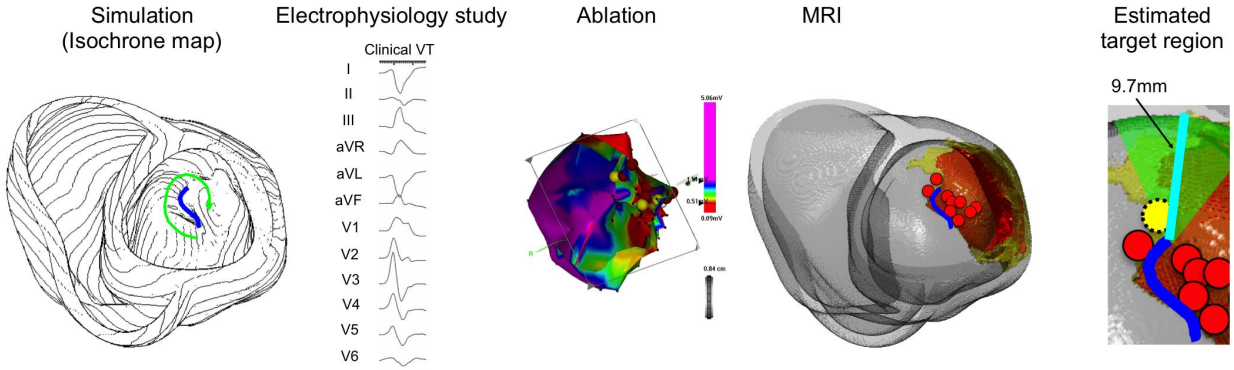

**Supplemental Videos**

**Supplemental Video 1. Simulation result of patient 1** (Figure 3a).

**Supplemental Video 2. Simulation result of patient 2** (Supplemental Figure 1b)**.**

**Supplemental Video 3. Simulation result of patient 3** (Figure 2a).

**Supplemental Video 4. Simulation result of patient 4** (Figure 4c).

**Supplemental Video 5. Simulation result of patient 6** (Figure 4b).

**Supplemental Video 6. Simulation result of patient 7** (Figure 2b).

**Supplemental Video 7. Simulation result of patient 8** (Figure 4a).

**Supplemental Video 8. Simulation result of patient 9** (Figure 2c).

**Supplemental Video 9. Simulation result of patient 10** (Supplemental Figure 1a).

**Supplemental Video 10. Simulation result of patient 11** (Supplemental Figure 2).

**Supplemental Video 11. Simulation result of patient 12** (Figure 3b).

**Supplemental Video 12. Simulation result of patient 13** (Figure 3c).